Wiley Online Library
Early View publication on www.wileyonlinelibrary.com
(issue and page numbers not yet assigned;
citable using Digital Object Identifier – **DOI**)

Phys. Status Solidi C, 1700069 (2017) / **DOI** 10.1002/pssc.201700069

physica status solidi c
www.pss-c.com
current topics in solid state physics

Intergranular barrier height fluctuations in polycrystalline semiconductors

C. Buono*, **F. Schipani, M. A. Ponce, and C. M. Aldao**

Institute of Materials Science and Technology (INTEMA), University of Mar del Plata and National Research Council (CONICET), Juan B. Justo 4302, B7608FDQ Mar del Plata, Argentina

Received 30 January 2017, accepted 8 March 2017
Published online 21 March 2017

Keywords electrical conduction, intergranular barriers, polycrystals, semiconductor interfaces, tunneling

* Corresponding author: e-mail cbuono@mdp.edu.ar, Phone: +54 223 481 6600, Fax: +54 223 481 0046

The punctual character and random nature of the impurity positions in depletion regions lead to inhomogeneities that can significantly affect the potential intergranular barriers at polycrystalline semiconductors and, in general, of potential barriers at any semiconductor interface. This would reflect in Arrhenius plots for the electrical conductivity that become curved due to fluctuations of the intergranular barrier heights. Experimental results for polycrystalline tin oxide can be fitted assuming thermionic emission conduction at grain boundaries with a Gaussian distribution of barrier height fluctuations. However, resorting to a computational numerical model, we found that spatial fluctuations in barrier heights due to the discreteness of the donors and their statistical distribution at the depletion region differ from a Gaussian distribution. The type of obtained fluctuations, considering thermionic emission conduction, cannot explain the Arrhenius plots for the electrical conductivity found experimentally, especially at low temperature. Conversely, the tunneling contribution to conduction, without resorting to fluctuations, presents the observed trends.

© 2017 WILEY-VCH Verlag GmbH & Co. KGaA, Weinheim

1 Introduction It is accepted from long ago that the electrical conduction in polycrystalline semiconductors is dominated by intergranular potential barriers that have a Schottky-type nature [1–9]. In particular, oxide semiconductors regularly present a dominant density of oxygen vacancies that confer a n-type character to the grains. Most researchers assume that electrical conduction is dominated by thermionic emission and then the conductance is generally described by [10]

$$G = G_0 \exp(-eV_s/kT), \quad (1)$$

where eV_s is the band bending, T the temperature, k the Boltzmann constant, and G_0 would be the electrical conductivity for no band bending. With Eq. (1) (i.e., assuming an Arrhenius relation) the barrier height ϕ, defined as $eV_S + E_C - E_F$, can be estimated; E_C is the conduction band minimum at the bulk and E_F is the Fermi level position. Thus, the conductance (ln G) versus the reverse function of temperature ($1/T$) should show a straight line [11]. Interestingly, experimental results on polycrystalline semiconductors do not regularly show such behavior as Arrhenius plots deviate from straight lines, especially at low temperatures [12].

To explain the observed temperature dependence of the electrical conductivity, a variety of reasons have been proposed. Among them, it has been claimed that the Arrhenius plots are curved due to fluctuations in barrier heights [13, 14]. Indeed, it is customary to model the electrostatic potential in a Schottky barrier by a one-dimensional quadratic potential, as it is obtained from a jellium of charge in the depletion region. However, the punctual character and random nature of the impurity positions lead to inhomogeneities that can significantly affect the conductivity.

In this theoretical and experimental work, we specifically study the effect of intergranular barrier height fluctuations on thermionic emission to explain the temperature dependence of the electrical conductivity in polycrystalline tin oxide. In particular, with a computational numerical model, we determine the spatial fluctuations in

© 2017 WILEY-VCH Verlag GmbH & Co. KGaA, Weinheim

barrier heights due to the discreteness of the donors and their statistical distribution at the depletion region. The effects on conductivity are then compared with experiments carried out on polycrystalline tin oxide films. We found that, as observed for a variety of polycrystalline semiconductors and semiconductor interfaces, experimental deviations from the Arrhenius behavior can be fitted assuming a Gaussian distribution of barrier height fluctuations. However, with numerical simulations, we determined that fluctuations do not present a Gaussian distribution and then they cannot explain the electrical conductivity found experimentally. Finally, we showed that the tunneling contribution accounts for the observed trends in the Arrhenius plots.

2 Electrostatic potential Although well known, for the sake of clarity, we now shortly review the intergranular double Schottky barriers as it is usually described without fluctuations. Although different types of defects are present in SnO_2, oxygen vacancies, which behave as electron donors, are considered dominant. There is an intergranular density of states that causes an exchange of electrons with the interior of the semiconducting grains, thus forming a space charge layer close to the surface. By changing the concentration and/or the energy distribution of the intergranular states, the space charge region is modulated and thus the conductivity is directly affected.

Conduction mechanisms have been interpreted in analogy to those in metal-semiconductor contact diodes. Accordingly, the electrical properties of polycrystalline semiconductors are usually described with a simple one-dimensional model representing the interface between two grains. By solving Poisson's equation for the depletion approximation, the relationship between the band bending and the depletion region width ω is [1]

$$V_s = \frac{eN_d}{2\varepsilon_r\varepsilon_0}\omega^2. \tag{2}$$

Figure 1 depicts the double Schottky barrier model that is generally accepted. Using Eq. (1) (i.e., assuming an Arrhenius relation) the band bending, or the barrier height ϕ, is regularly estimated. Indeed, by plotting the conductance ($\ln G$) versus the reverse function of temperature ($1/T$), an activation energy value is obtained [11]. However, the

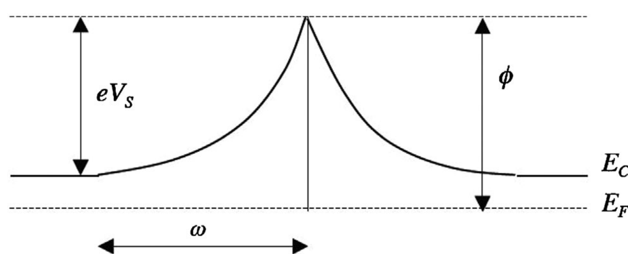

Figure 1 Diagram for the intergranular double-Schottky barrier model. The band bending is eV_S, ϕ the height of the barrier, and ω is the width of the depletion region.

underlying assumption in the above analysis is that the potential barrier has the same height and shape along the whole interface. In fact, this is an incorrect picture because the potential barrier arises from the Coulomb potential due to all present charges and then fluctuations must be present. The relevance of these fluctuations will be analyzed after presenting some experimental results.

3 Experimental Commercial high-purity SnO_2 (Aldrich, medium particle size 0.4 μm) was ground until a medium particle size of 0.130 μm was obtained as determined using the intersection method from SEM images. The resulting powder was thermally treated up to 380 °C using a heating rate of 1 °C min^{-1}. Later, the powder was cooled up to 25 °C and a paste was prepared with an organic binder (glycerol). The used solid/organic binder ratio was 1/2, and no dopants were added. Thick, porous film samples were made by painting onto insulating alumina substrates on which electrodes with an interdigitated shape (platinum film 200 nm thick, after 25 nm of titanium as an adhesion layer) were deposited by sputtering. The alumina substrates were 96% dense.

After painting, samples were thermally treated for 1 h in air at 100 °C. This treatment was performed in order to evaporate the organic binder and to improve the films adhesion on the alumina substrate. Later, samples were thermally treated up to 380 °C for 1 h in an air atmosphere using a heating rate of 1 °C min^{-1}. After thermal treatment, the film was cooled down to 25 °C. Finally, some of the samples were kept at 380 °C for 4 h in a N_2 atmosphere with 5% H_2. Samples were labeled S_{O2} (samples only exposed to dry air) and S_{H2} (samples exposed to hydrogen).

To image the tin oxide surfaces, a JEOL JSM 6460-S scanning electron microscope was employed. From SEM characterization of film surfaces, shown in Fig. 2a, porous microstructure composed of a relatively wide distribution of grain sizes was noticed (130 nm). By SEM cross-section examination, it was determined that the film-thickness was approximately 150 μm (Fig. 2b).

After thermals treatment in different atmospheres, films were characterized using X-ray diffraction, XRD – Philips (PW1830), with a PANalytical X'Pert PRO diffraction system employing CuK_α radiation ($\lambda = 0.1542$ nm) at 40 kV and 40 mA. Samples were scanned between 20 and 80° with a step size of 0.02°. Figure 3a shows the XRD pattern of a film before treatment. In their original state, the chemical composition and crystal structure of the films match very well with that of tetragonal rutile SnO_2. Most of the observed peaks correspond to the diffraction planes typical of the SnO_2 cassiterite phase (PDF no. 01-071-0652). The diffractogram also shows other minor peaks that can be attributed to the substrate: alumina (PDF no. 00-011-0661) and Ti_2O (PDF no. 01-73-1582) as an adhesion layer consisting of 25 nm of titanium was deposited in making the electrodes. The codes correspond to the International Centre for Diffraction Data (ICCD) (1998) Powder diffraction file database, Newtown Square (USA) [15]. No changes in

© 2017 WILEY-VCH Verlag GmbH & Co. KGaA, Weinheim

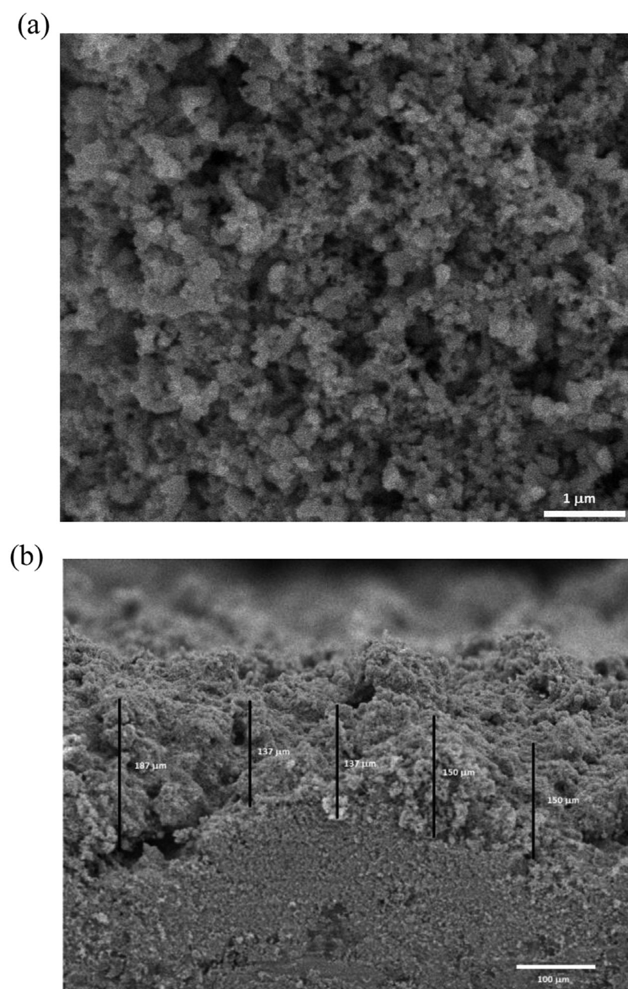

Figure 2 (a) SEM micrograph of the film showing a porous structure with an average grain size of 0.130 μm as determined using the intersection method. (b) Micrograph of the film cross-section that presents an average thickness of ≈150 μm.

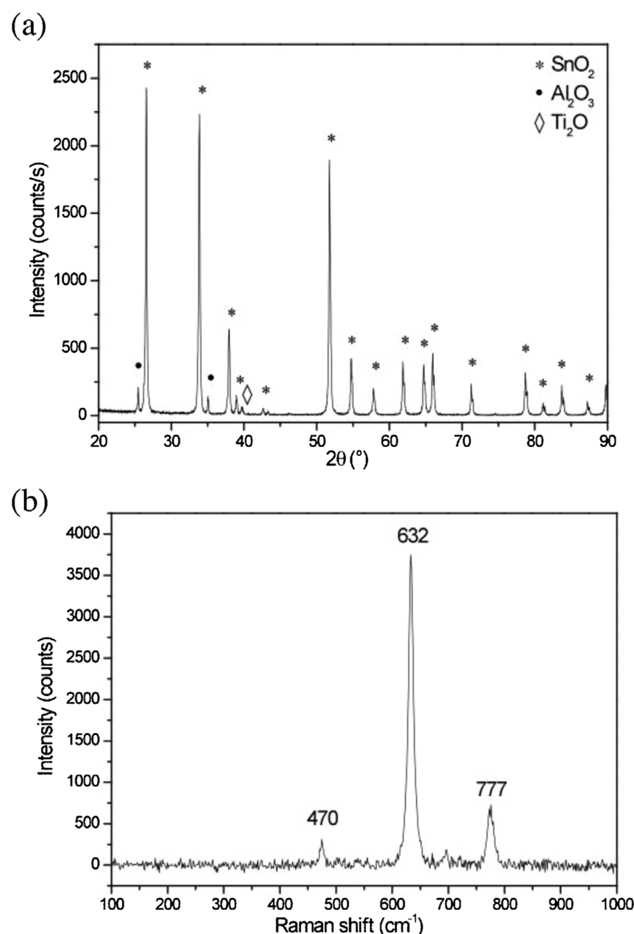

Figure 3 (a) X-ray diffraction pattern in the range 20–80° (2 h). A tin oxide tetragonal crystalline system is only observed in the powder used in our samples. (b) Raman spectrum of the film (initially conformed/without gas treatments).

phases or composition were observed after oxygen or hydrogen treatment.

Raman spectroscopy was carried out to verify that the material composition does not change after film conformation. The spectra were recorded at room temperature with a Renishaw in Via Reflex spectrometer system equipped with charge-coupled device (CCD) detector of 1040 × 256 pixels and coupled to a Leica microscope with a 100× (0.9 NA) Leica metallurgical objective. An Ar laser line (514 nm, 50 mW) was used as excitation source in combination with a grating of 2400 grooves/mm. Figure 3b shows Raman spectrum for the film before gas treatments. The film shows the bands characteristics of SnO_2. Peaks at 470, 632, and 777 cm^{-1} have been assigned to the E_g, A_{1g}, and B_{2g} vibrational modes of SnO_2 in tetragonal rutile structure, respectively [16, 17]. Also, using this technique, no changes were observed after oxygen or hydrogen treatment (spectra are not presented, they are similar to that of Fig. 3b).

After preparation, samples were placed in the measuring cell, and inside an isolating recipient with liquid nitrogen for cooling purposes. Gaseous nitrogen was flown the entire time to ensure no contact with ambient oxygen. The lowest temperature reached was −123 °C and then increased separating the sample from the liquid nitrogen. External heaters were used for higher temperatures, without removing the sample. Measurements were made after reaching steady state at different temperatures. An Agilent 34401A multimeter was used for the DC electrical conductance measurements. Given the resistance values, we used the two-point resistance measurement method. Finally, a Hewlett Packard impedance analyzer model 4184A was used for capacitance measurements.

Figure 4 shows the conductance measured in nitrogen of the oxygen treated (S_{O2}) and hydrogen treated (S_{H2}) samples versus the inverse of temperature, from 150 up to 330 K. In this temperature range, the conductivity change for the S_{H2} sample as a function of temperature is relatively small; the activation energy at the highest temperatures can be estimated 0.19 ± 0.01 eV. The S_{O2} sample shows a much

 © 2017 WILEY-VCH Verlag GmbH & Co. KGaA, Weinheim

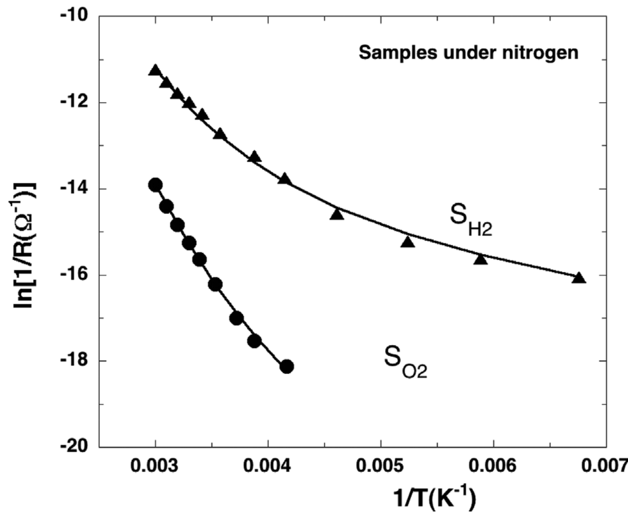

Figure 4 Conductance for the hydrogen (S_{H2}) and oxygen (S_{O2}) treated samples as a function of temperature from 150 up to 330 K. Lines are fittings to the experimental results assuming thermionic emission conduction.

lower conductance and the activation energy at the highest temperatures corresponds to an activation energy of $0.41 \pm 0.02\,\text{eV}$. Higher temperatures were not explored to avoid gas adsorption/desorption that can take place during the heating and cooling processes. Both Arrhenius plots show a curvature at low temperatures. In the case of S_{O2}, we could not measure at low temperatures as the conductivity was below the detection limit. Similar results have been obtained by many authors and for a variety of polycrystalline semiconductors [18–24].

4 Potential height fluctuations The thermionic emission theory for a Schottky barrier leads to the following current density/voltage relation [25]

$$J = A^*T^2 \exp\left(-\frac{\phi}{kT}\right)\left[\exp\left(\frac{eV}{kT}\right) - 1\right], \tag{3}$$

where A^* is the Richardson constant. Thus, the conductance for an applied voltage $V << kT$ can be computed using dJ/dV

$$G = \frac{eA^*}{k} T \exp(-\phi/kT). \tag{4}$$

Many researchers assume that the fluctuations of barrier heights present a Gaussian distribution of the form [25–31]

$$P(\phi) = \frac{1}{u\sqrt{2\pi}} \exp\frac{-(\phi-\phi_0)^2}{2u^2}, \tag{5}$$

where ϕ_0 is the mean value and u the standard deviation of the barrier height. Thus, the electrical conductance, assuming a thermionic emission mechanism, can be calculated with

$$G = \frac{eA^*}{k}\int_0^\infty P(\phi)F(\phi)d\phi, \tag{6}$$

where $F(\phi) = \exp(-\phi/\text{kT})$.

According to the geometry of our sensors, the electrical resistance can be related to that of semi-infinite electrodes, coplanar with a gap separating them. With the results of Ref. [32] we can calculate the resistance for our geometry

$$R \approx \frac{\pi}{l\sigma \sinh^{-1}(2e/D)}, \tag{7}$$

where D is the width of the inter-electrode pathway, e is the film thickness, l is the length of the electrodes, and s is the conductivity. For our geometry, $R \approx \pi/(3l\sigma)$ and then the measured conductivity is $\sigma = \pi G/(3l)$ [33]. To compare the experimental results with those resulting from a thermionic emission conduction, we have to consider the presence of grains and intergranular barriers. The conductivity of a single cubic grain of size d would be Jd/V as there is an intergrain barrier per grain. Therefore, the conductance in terms of the current density and the applied voltage to a single intergranular barrier is $G \approx 3dlJ/(\pi V)$. Equation (7) indicates that the resistance presents a weak dependence with the film thickness; for example, a sample 20% thicker implies a lower value or R of about 7%. Since we are dealing with a varying thickness with positive and negative fluctuations of about 20%, the expected error is even smaller. On the other hand, the temperature dependence of Fig. 4 is determined with the same film and then the resistances at all temperatures are weighted by the same factor. This error is not relevant here, as it does not affect any of the conclusions of this work.

Figure 4 shows the fitting of the experimental results assuming thermionic emission conduction by means of Eqs. (5) and (6). The mean value of the barrier height ϕ_0 and its standard deviation u are adjustable parameters. Reported fittings correspond to $f_0 = 0.95\,\text{eV}$ and $u = 0.143\,\text{eV}$ for the sample S_{H2}, and $\phi_0 = 0.95\,\text{eV}$ and $u = 0.126\,\text{eV}$ for the sample S_{O2}. Results are very sensitive to the fitting parameters to the point that uncertainties in their determination are below 1%. Interestingly, experiments are reproduced by changing its standard deviation and using the same mean value of the barrier height. This is consistent with a previous work that shows that samples exposed to different gas treatments and measured in the same atmosphere present different conductance but the same barrier height [34].

The model indicates that larger deviations in the barrier height directly affect the conductance, especially at low temperatures. The reason is that, as the barrier height deviation increases, the transfer of electrons across the interface occurs at regions with lower barriers. This can be clearly detected by plotting the integrand in Eq. (6). In Fig. 5, curve (a) corresponds to sample S_{H2} and curve (b) to

© 2017 WILEY-VCH Verlag GmbH & Co. KGaA, Weinheim

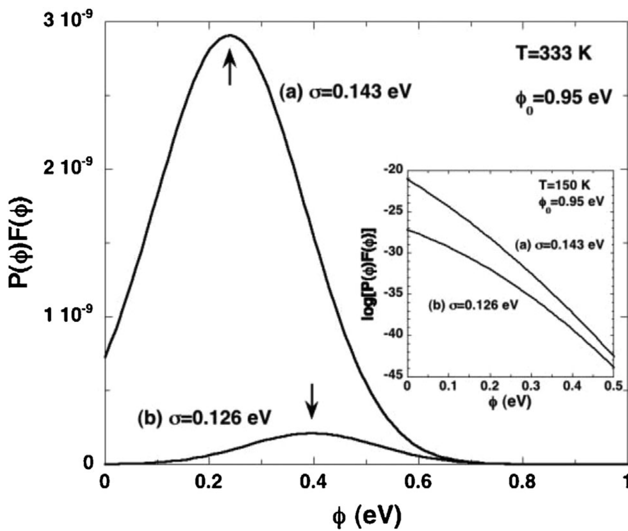

Figure 5 Integrand $P(\phi)F(\phi)$ of Eq. (4) as a function of barrier height. Sample conductivity is proportional to the integral of $P(\phi)$ $F(\phi)$. As the dispersion in the barrier heights increases, electrons mostly overcome the barrier at places of the interface with barrier heights much lower than its mean value. The inset shows that at low temperatures most electrons cross the interface at places were the barrier is close to be zero. Arrows indicate the $P(\phi)F(\phi)$ maxima.

sample S_{O2} at 333 K. It is clearly seen that electrons mostly overcome the barrier at places where the barrier is remarkably smaller than its mean value. The product $P(\phi)F(\phi)$ presents a maximum at ϕ_{max} that can be analytically determined,

$$\phi_{max} = \phi_0 - \frac{u^2}{kT}. \quad (8)$$

The arrows in Fig. 5 show the position of ϕ_{max}. For large values of the dispersion u and/or low temperatures, Eq. (8) predicts a negative ϕ_{max}, which is mathematically correct but it has no physical sense. This result indicates that most electrons overcome the barrier in the proximities of $\phi = 0$ as shown in the inset of Fig. 5.

In fitting experimental data, as we did in Fig. 4, two main assumptions are taken for granted: (i) the thermionic emission is the dominating electrical conduction mechanism and (ii) fluctuations of barrier heights present a Gaussian distribution. In principle, a Gaussian distribution seems a sound choice. However, this distribution is only valid for independent events; this is not the present case. As clearly stated in Ref. [35], a Gaussian distribution for barrier heights represents a first choice or a first approximation to model nonuniformities in the interface potentials. We were then motivated to check the validity of assumption (ii).

5 Numerical simulations We calculated the electrostatic potential due to a double Schottky barrier, arising from a random distribution of dopants in the depletion regions [36, 37]. Following Mahan [36], we approximate the electrostatic potential of a random distribution of point charges (ionized dopants). We built a parallelepiped of size $x \times y \times z$ shown schematically in Fig. 6. The width of the parallelepiped z is 2ω, where ω is the depletion region width from Eq. (2). We randomly distribute a finite number of donors inside the parallelepiped in $-\omega \leq z \leq \omega$ except in the plane $z = 0$ that corresponds to the grain-boundary. Then, we associate to each charge an equal and opposite charge in the interface, at the grain-boundary; with this arrangement there is charge neutrality (see Fig. 6). For our simulations we use a mesh of $200 \times 200 \times 100$ and distribute approximately 1150 charges using a barrier height $\phi_0 = 0.8$ eV and a doping concentration $N_d = 10^{24}\,m^{-3}$ which are typical values in tin oxide.

The barrier height for a given position in the plane of the barrier is defined as the maximum electrostatic potential in the direction normal to this plane (z direction) for every point in the parallelepiped. The Coulomb ($1/r$) potential does not include the contributions of the core electrons of the donors, they are bound electrons at the immediate proximity of the point charge. An approximate potential can be generated by cutting off the $1/r$ potential at a distance R_s, which is close to the Bohr radius [38, 39]. In our simulations, we replace the potential with a constant inside this radius. The choice of R_s was made by using the next argument. If we consider the charge density as constant within R_s, the potential will behave inversely with the distance outside R_s, and quadratically inside R_s. Therefore, we choose R_s such that the constant potential value inside is approximately the potential reached if the charge were distributed uniformly in R_s. We found that R_s must be approximately 14 Å for tin oxide. Taking into account this cut off, we compute the electrostatic potential in every point of the system as the sum of the Coulomb potentials generated by all charges. As above, it is expected that this approximation also leads to an error by excess.

A sample subsection of the barrier height as a function of position in the y direction for a fixed x is shown in Fig. 7 on a mesh of $200 \times 200 \times 100$ points with a doping concentration $N_d = 10^{24}\,m^{-3}$ and an average barrier height $\phi_0 = 0.8$ eV. Periodic boundary conditions were used to

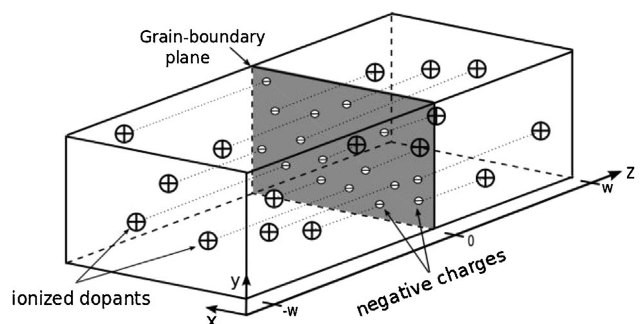

Figure 6 Schematic diagram of the numerical simulation geometries and the arrangement of the punctual charges.

© 2017 WILEY-VCH Verlag GmbH & Co. KGaA, Weinheim

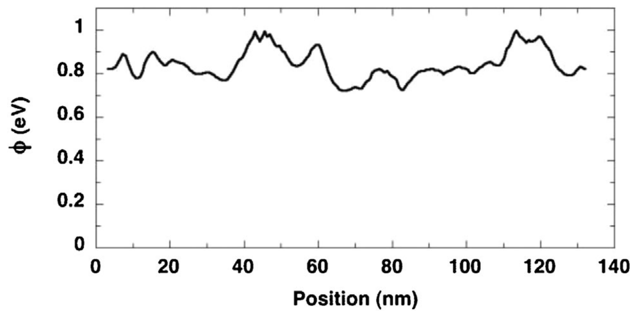

Figure 7 A sample portion of the barrier height as a function of the position for a back-to-back Schottky barriers. The doping concentration is $N_d = 10^{24}\,m^{-3}$ and the average barrier height is $\phi_0 = 0.8$ eV.

avoid edge effects. Other doping concentrations, doubly charged dopants, other sizes of the parallelepiped and barrier heights were tested to check the finite size effects and the mesh sensitivity of the results; we found that fluctuations do not vary substantially.

The relative frequency or normalized probability density, for 20 observations, is shown as empty circles in Fig. 8. To do this, data were binned in intervals of 1 meV. The probability density has a maximum close to ϕ_0 and a standard deviation of $\approx$0.1 eV due to fluctuations. At first sight, the probability density looks quite similar to a Gaussian distribution. Fitting with a Gaussian (the solid line in Fig. 8) shows that this approximation fails for small and large values of the barrier heights due to a slight asymmetry of the found distribution.

It seems that a Gaussian approximation is not a bad starting point as it reproduces quite well the central part of the distribution. However, the inset of Fig. 8 shows the

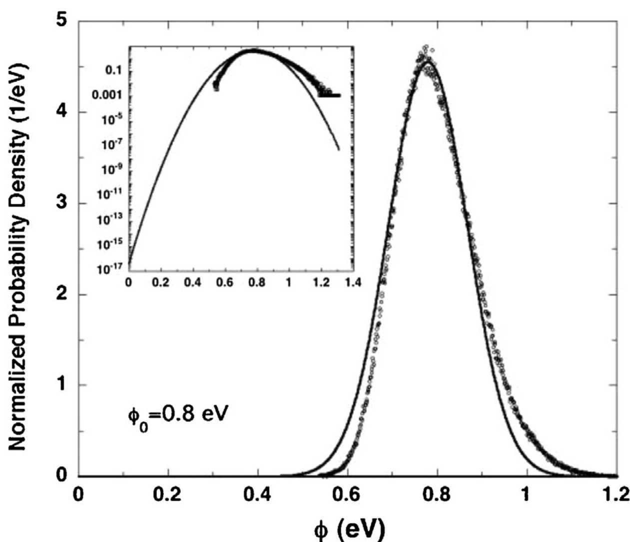

Figure 8 The normalized barrier height density distribution in eV^{-1}, as a function of barrier height in a linear–linear scale. The solid line is the fitting with a Gaussian function. The inset shows the same plot in a log-linear scale.

probability density for the barrier height in a log-linear scale, making more evident the difference between numerical simulation results and the approximation. In particular, the simulation corresponds approximately to an interface equivalent to a square with a side of 0.6 μm, which is a much larger surface than the typical intergrains of our films. Interestingly, the barrier height is never below 0.53 eV or above 1.31 eV.

In nature, many outcomes that depend on the sum of independent events approximate the Gaussian distribution. This is valid if respected the assumption that the sample is obtained containing a large number of observations, each observation being randomly generated in a way that does not depend on the values of the other observations and then they are uncorrelated. This is not valid in our case because barrier heights do not adopt uncorrelated values since potentials cannot change abruptly; note that the barrier height arises from summing Coulomb potentials. The point is that if barrier heights follow a Gaussian distribution, there would be a non-zero probability of having very low barriers. For example, for a Gaussian distribution, the probability of having a zero barrier height if $\phi_0 = 0.95$ eV and $u = 0.143$ eV, needed to fit the results corresponding to sample S_{H2}, is 7.3×10^{-10}. Thus, for an intergrain of $100 \times 100\,nm^2$, the potential would be zero in an area equivalent to a square with a side of 2.7×10^{-3} nm, which has no physical sense. In other words, there is no charge distribution that is able to generate the needed potential. Our results show that the probability density for the barrier heights differs significantly from a Gaussian as $|\phi - \phi_0|$ *increases (see Fig. 8). Furthermore, there is a cut off in the probability density for small barrier heights, indicating that very low barriers are not present in the system.*

It could be argued that the probabilities of having very low barriers are very small and then the observed differences are not relevant. This is the point of the present work, the inclusion of low barrier values, even with low probability, can notably affect the conductance, since electrons mostly overcome the barrier at its lowest values. In Fig. 9 we plot the product $P(\phi)F(\phi)$, directly related to conductivity through Eq. (6), for a temperature of 333 K, as in the previous section, but now we use the barrier height distribution $P(\phi)$ obtained with our numerical simulation (results of Fig. 8). Figure 9 shows that, while the main contribution to conduction corresponds to barrier heights around ϕ_{max}, below the average value ϕ_0, the difference $\phi_0 - \phi_{max}$ is remarkably smaller compared to the results found in Fig. 5 (where the probability density was considered Gaussian). In the inset of Fig. 9, we show the product $P(\phi)F(\phi)$ for a lower temperature, $T = 150$ K, the maximum ϕ_{max} decreases but it does not differ considerably from the result corresponding to $T = 333$ K.

A simple model, as the one we presented, captures the essence of the problem showing that fluctuations of barrier heights due to the punctual character and random nature of the impurity positions at depletion regions do not present a Gaussian distribution. With the found type of fluctuations it

© 2017 WILEY-VCH Verlag GmbH & Co. KGaA, Weinheim

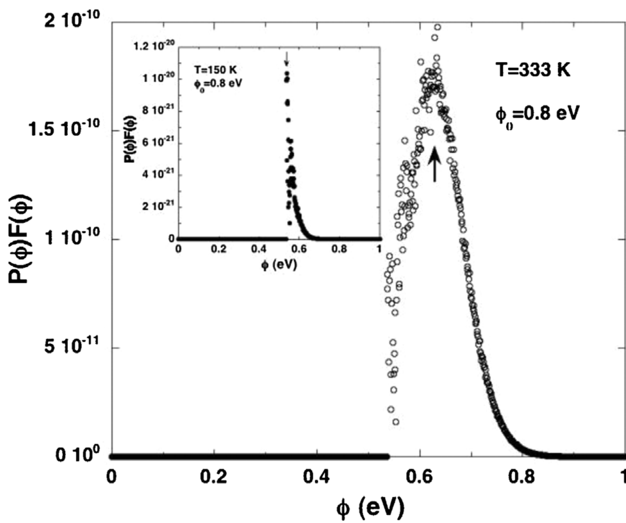

Figure 9 $P(\phi)F(\phi)$ using the barrier height distribution $P(\phi)$ obtained with our numerical simulation (results of Fig. 7). Sample conductivity is proportional to the integral of $P(\phi)F(\phi)$. Note that the contributions to the conductivity arise from narrow values of barrier heights. The inset shows that at low temperatures electrons cross the interface at places with not very different barrier heights. Arrows indicate the $P(\phi)F(\phi)$ maxima.

is not possible to fit experimental results assuming thermionic emission as the dominating electrical conduction mechanism.

It is known that the actual carrier concentration and mobility are a function of temperature. However, their dependences on temperature partially compensate each other and the resulting effect on conductivity is not enough to reproduce experiments [40]. On the other hand, usually a so-called bricklayer model with cubic-shaped grains of identical size is assumed, which constitutes a simplification of the real microstructure. The actual randomness of the structure produces preferential paths for the electrical current leading to a lower global resistance, but the error made is around 10%, which is very small to be responsible for the observed results [41]. Other explanations for the curvature in the log (conductivity) v. $1/T$ plots must be proposed.

6 Tunneling contribution to conduction

It is known that it is possible for electrons with energies below the top of a barrier to penetrate it by quantum-mechanical tunneling. Tunneling probability increases with the electron energy as electrons find a thinner and lower barrier. In opposition, the number of electrons decreases with energy. Thus, there is a maximum contribution at a given energy above the bottom of the conduction band. This contribution to electrical conduction is known as thermionic-field emission [42].

As mentioned, a double Schottky barrier model is widely accepted to describe polycrystalline semiconductor intergrains. However, many researchers consider grain boundaries of essentially zero width, while others take into account a non-negligible disordered layer at the grain boundaries, such that the electron transport occurs in two steps. Since the main conclusions will not differ, for the sake of simplicity we will adopt here the second assumption.

The tunneling current can be calculated with

$$J_{\text{tunneling}} = \frac{A^*T}{k}\int_0^{\phi} F(E)P(E)dE, \quad (9)$$

where $F(E)$ is now the Fermi-Dirac distribution and $P(E)$ is the transmission probability, which can be determined by means of the Wentzel–Kramer–Brillouin approximation [43]. Typical dopant concentrations make thermionic-field emission the most relevant conduction mechanism in many cases.

Figure 10 shows the expected conductivity for the same parabolic barrier in all cases without fluctuations and height equal to 0.95 eV (the same as the mean value used in our fittings assuming thermionic emission conduction) and several dopings. In all cases shown the tunneling contribution is the dominant conduction mechanism in the studied temperature range. Indeed, at $T = 333$ K the thermionic contribution is about 400 times smaller than that corresponding to tunneling for the lowest studied doping. Experimental data of Arrhenius plots on various semiconductors, as found in Ref. [16], show a similar trend. In Fig. 10 we also include our experimental data of Fig. 4. We do not present fittings using other barrier heights, but it is seen that, with the used value, results can be reproduced quite well.

In calculating the electrical conductance assuming thermionic emission, see Eq. (6), $P(\phi)$, which is the

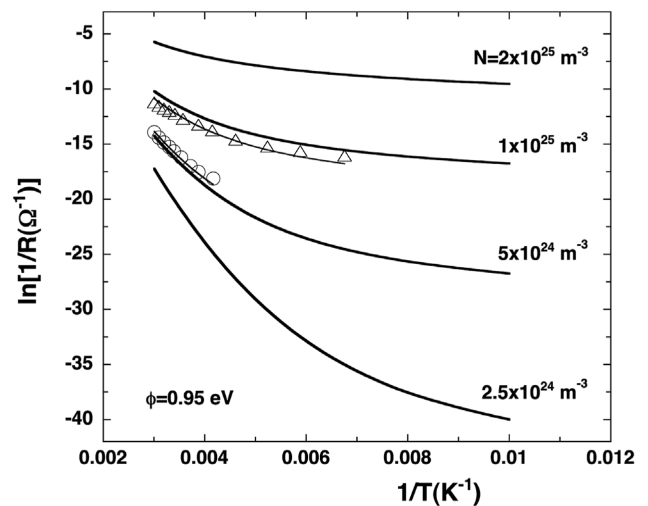

Figure 10 Arrhenius plots of electrical conductivity in which thermionic and thermionic-field contributions are included. We considered parabolic barriers without fluctuations with height equal to 0.95 eV. Experimental results of Fig. 4 are also shown with fittings corresponding to dopings equal to S_{H2}, is 9×10^{24} for S_{H2} and $5.3 \times 10^{24}\,\text{m}^{-3}$ for S_{O2}.

© 2017 WILEY-VCH Verlag GmbH & Co. KGaA, Weinheim

distribution of barrier heights due to fluctuations, plays the same role than $P(E)$, which is the transmission probability, in Eq. (9). Interestingly, $P(E)$ presents, for $E < \phi_0$, a dependence with E very similar to a Gaussian. At low temperatures most electrons overcome the barrier at energies below the barrier top. Thus, using a Gaussian as a weighting function for thermionic emission, the observed temperature dependence of Arrhenius plots can be fitted. However, the tunneling contribution is the dominant conduction mechanism for large-doped samples, especially at low temperatures, and also reproduces the observed Arrhenius plots.

6 Conclusions We have analyzed the effects of intergranular barrier height fluctuations on thermionic emission in the electrical conductivity of polycrystalline tin oxide. We found that experiments carried out on polycrystalline tin oxide films can be reproduced with a Gaussian distribution for the barrier height fluctuations using only a thermionic mechanism. Then, we determined the spatial fluctuations in barrier heights due to the discreteness of the donors and their statistical distribution at the depletion region of a back-to-back Schottky barrier with a computational numerical model. Interestingly, we found that barrier height fluctuations do not follow a Gaussian distribution. In particular, fluctuations do not generate very low barrier heights. Thus, fitting with a Gaussian distribution leads to an artefact. Researchers adopt a Gaussian distribution because it seems to be a reasonable distribution. The problem is that it is not correct to apply it to this case. The reason is that barrier heights do not come from independent events. In short, for a typical grain size, the probability of having a zero barrier height is practically null. Conversely, a Gaussian distribution always leads to zones with a zero barrier height. Even though the area is very small, it would occur. Since what is relevant is its product with a Boltzmann distribution, it results that the main contribution, at low temperatures, comes from zones with very low barriers, which in fact are nonexistent. We conclude that the observed Arrhenius plot deviations from straight lines, especially at low temperatures, cannot be explained resorting to barrier height fluctuations because they do not present a distribution that could be responsible for the observed temperature conductivity dependence assuming thermionic emission. Therefore, other causes must be explored. Among them, the inclusion of the tunneling contribution appears as a must as many experiments are carried out using samples with large dopings for which tunneling not only is non-negligible but also is the dominant conduction mechanism. The observed temperature and doping dependences of the tunneling contribution nicely reproduce the trends on experimental observations for a variety of semiconductors.

Acknowledgements This work was partially supported by the National Council for Scientific and Technical Research (CONICET) of Argentina and the National University of Mar del Plata (Argentina). We thank Daniel Mirabella and Alejandro Uriz for stimulating discussions.

References

[1] M. J. Madou and R. Morrison, Chemical Sensing with Solid State Devices (Academic, San Diego, 1989).
[2] G. D. Mahan, L. M. Levinson, and H. R. Phillipp, J. Appl. Phys. **50**, 2799 (1979).
[3] G. E. Pike, Phys. Rev. B **30**, 795 (1984).
[4] G. Blatter and F. Greuter, Phys. Rev. B **33**, 3952 (1986).
[5] N. Barsan and U. Weimar, J. Phys.: Condens. Matter. **15**, R813 (2003).
[6] N. Yamazoe, Sens. Actuators B **108**, 2 (2005).
[7] M. Batzill and U. Diebold, Prog. Surf. Sci. **79**, 47 (2005).
[8] J. J. Velasco-Vélez, U. Kunze, T. Hass, and T. Doll, Phys. Status Solidi A **207**, 924 (2010).
[9] D. R. Leitr, M. Cilense, M. O. Orlandi, P. R. Bueno, E. Longo, and J. A. Varela, Phys. Status Solidi A **207**, 457–461 (2010).
[10] W. Gopel and K. Schierbaum, Sens. Actuators B **26**, 1 (1995).
[11] F. Schipani, C. M. Aldao, and M. A. Ponce, AIP Adv. **2**, 032138 (2012).
[12] M. S. Castro and C. M. Aldao, Appl. Phys. Lett. **63**, 1077 (1993).
[13] R. T. Tung, J. P. Sullivan, and F. Schrey, Mater. Sci. Eng. B **14**, 266 (1992).
[14] F. E. Cimilli, M. Sağlam, H. Efeoğlu, and A. Türüt, Physica B **404**, 1558 (2009).
[15] IICFD. Powder Diffraction File Database (Campus Boulevard Newtown Square, PA, USA, 1998).
[16] J. X. Wang, D. F. Liu, X. Q. Yan, H. J. Yuan, L. J. Ci, Z. P. Zhou, Y. Gao, L. Song, L. F. Liu, W. Y. Zhou, G. Wang, S. S. Xie, Solid State Commun. **130**, 89 (2004).
[17] M. Ristić, M. Ivanda, S. Popović, and S. Musić, J. Non-Cryst. Solids **303**, 270 (2002).
[18] Y. Kajikawa, J. Appl. Phys. **112**, 123713 (2012).
[19] M. V. Garcia-Cuenca, J. L. Morenza, and J. Esteve, J. Appl. Phys. **56**, 1738 (1984).
[20] I. Gunal and M. Parlak, J. Mater. Sci.: Mater. Electron. **8**, 9 (1997).
[21] A. P. Roth and D. F. Williams, J. Appl. Phys. **52**, 6685 (1981).
[22] M. Regragui, V. Jousseaume, M. Addou, A. Outzourhit, J. C. Bernede, and B. El Idrissi, Thin Solid Films **397**, 238 (2001).
[23] N. Yamazoe, J. Fuchigami, M. Kishikawa, and T. Seiyama, Surf. Sci. **86**, 335 (1979).
[24] A. V. Sukach, V. V. Tetyorkin, and N. M. Krolevec, Semicond. Phys. Quantum Electron. Optoelectron. **13**, 221 (2010).
[25] E. H. Rhoderick and R. H. Williams, Metal-Semiconductor Contacts, 2nd edn. (Oxford Science, Oxford, U.K., 1988).
[26] J. H. Werner and H. H. Güttler, J. Appl. Phys. **69**, 1522–1533 (1991).
[27] S. K. Tripathi and M. Sharma, J. Appl. Phys. **111**, 074513 (2012).
[28] Y. Kajikawa, K. Okamura, Y. Inoko, and H. Mizuki, J. Appl. Phys. **112**, 123712 (2012).
[29] Y. Kajikawa, J. Appl. Phys. **114**, 043719 (2013).
[30] W. Mtangi, F. D. Auret, C. Nyamhere, P. J. Janse van Rensburg, M. Diale, and A. Chawanda, Physica B **404**, 1092 (2009).

© 2017 WILEY-VCH Verlag GmbH & Co. KGaA, Weinheim

[31] A. Bobby, S. Verma, K. Asokan, P. M. Sarun, and B. K. Antony, Physica B **431**, 6 (2013).
[32] D. Pascal, P Dansas, C. Bru, and S. Laval, Semicond. Sci. Technol. **4**, 633 (1989).
[33] F. Schipani, M. A. Ponce, E. Joanni, F. J. Williams, and C. M. Aldao, J. Appl. Phys. **116**, 194502 (2014).
[34] C. M. Aldao, F. Schipani, M. A. Ponce, E. Joanni, and F. J. Williams, Sens. Actuators B **193**, 428 (2014).
[35] D. J. Thompson and H. C. Card, J. Appl. Phys. **54**, 1976 (1983).
[36] G. D. Mahan, J. Appl. Phys. **55**, 980 (1984).
[37] M. van Schilfgaarde, J. Vac. Sci. Technol. B **8**, 990 (1990).
[38] D. Arnold and K. Hess, J. Appl. Phys. **61**, 5178 (1987).
[39] T. H. Ning and C. T. Sah, Phys. Rev. B **4**, 3468 (1971).
[40] C. G. Fonstad and R. H. Rediker, J. Appl. Phys. **42**, 2911 (1971).
[41] G. Dezanneau, A. Morata, A. Tarancón, F. Peiró, and J. R. Morante, Solid State Ion. **177**, 3117 (2006).
[42] S. M Sze, Physics of Semiconductor Devices (Wiley, New York, 1981).
[43] C. R. Crowell and V. L. Rideout, Solid State Electron. **12**, 89 (1969).

 © 2017 WILEY-VCH Verlag GmbH & Co. KGaA, Weinheim